# Tailoring magnetocrystalline anisotropy and anisotropic magnetocaloric effect in Ni-doped $Fe_3GaTe_2$ single crystals

Luozhao Zhang,[1] Liqiang Zeng,[2] Jinbo Yang,[1] Yongfeng Mei,[1,3,4] Zhongchong Lin,[2,5,*] Zhigao Huang,[2,5] and Jizhai Cui[1,3,4,†]

[1]*State Key Laboratory of Surface Physics & International Institute for Intelligent Nanorobots and Nanosystems, College of Intelligent Robotics and Advanced Manufacturing, Fudan University, Shanghai 200438, China*

[2]*Fujian Provincial Key Laboratory of Quantum Manipulation and New Energy Materials, College of Physics and Energy, Fujian Normal University, Fuzhou 350117, China*

[3]*Zhejiang Key Laboratory of Extreme Environment Functional Materials, Yiwu Research Institute of Fudan University, Yiwu 322000, Zhejiang, China*

[4]*Shanghai Key Laboratory of Metasurfaces for Light Manipulation, Fudan University, Shanghai 200433, China*

[5]*Fujian Provincial Engineering Technical Research Centre of Solar-Energy Conversion and Stored Energy, Fuzhou 350117, China*

(Received 30 November 2025; revised 25 April 2026; accepted 8 June 2026; published 6 July 2026)

The regulation of magnetic anisotropy in two-dimensional (2D) van der Waals (vdW) ferromagnets is critical for enabling spintronic and solid-state cooling applications, yet the microscopic doping mechanism remains poorly understood, as conventional ideal-lattice models fail to reconcile the moderate structural and magnetic evolution observed in experiments. In this work, we investigate Ni-doped $Fe_3GaTe_2$, a room-temperature 2D ferromagnet, combining systematic magnetization measurements and first-principles calculations based on the realistic defective lattice structure of $Fe_3GaTe_2$. We demonstrate an intrinsic defect-assisted occupation mechanism: Ni dopants preferentially substitute the preexisting interstitial Fe atoms in the vdW gap rather than inserting into empty interlayer sites. This mechanism accounts well for all our experimental observations, including the minor *c*-axis contraction, the 80% reduction of magnetocrystalline anisotropy energy with preserved out-of-plane easy axis, and the monotonic decrease of Curie temperature ($T_C$) and saturation magnetization. Furthermore, we demonstrate that Ni doping effectively tunes the anisotropic magnetocaloric effect: The anisotropy of magnetic entropy change decreases from 0.68 to 0.29 $J\,kg^{-1}\,K^{-1}$, while the relative cooling power exhibits a nonmonotonic evolution, reaching an optimal value of 156 $J\,kg^{-1}$ at 4.6% Ni doping. The evolution of critical exponents *n* and *m* confirms that Ni doping introduces magnetic disorder, broadening the magnetic phase transition. Our results resolve the discrepancy between ideal-lattice theoretical predictions and experimental observations, providing a clear microscopic picture for anisotropy engineering in 2D magnets.

DOI: 10.1103/k713-wl4g

## I. INTRODUCTION

Magnetic anisotropy lies at the heart of two-dimensional (2D) van der Waals (vdW) magnetism: It not only overcomes the Mermin-Wagner bound to stabilize long-range magnetic order in the 2D limit [1] but also serves as the core knob to tailor the functional properties of these materials. Its origins are primarily magnetocrystalline anisotropy, dominated by spin-orbit coupling (SOC) interactions, and magnetic shape anisotropy, dominated by long-range dipole-dipole interactions. The regulation of magnetic anisotropy is therefore critical for both exploring exotic new spin orders and enabling practical device applications. Specifically, in spintronics, anisotropic control enables low-power, high-density devices, ranging from anisotropy-tunable heterostructures to skyrmion-based memory systems [2–5]. In magnetocaloric refrigeration, anisotropy dictates the efficiency of the magnetic entropy change $\Delta S_M$ and phase transition behavior, enabling giant rotational cooling effects in engineered materials [6–9]. To this end, various approaches, such as interfacial engineering [10], chemical doping [11,12], and strain [13], have been developed to effectively tune anisotropy.

The discovery of 2D vdW ferromagnets has driven rapid advances in this field, yet most early candidates, such as $CrI_3$ ($T_C \sim 60$ K) and $Fe_3GeTe_2$ ($T_C \sim 230$ K), suffer from low Curie temperatures, significantly limiting their practical applications [14–16]. This persistent limitation was recently addressed by the discovery of $Fe_3GaTe_2$ [17], a prototypical room-temperature vdW ferromagnet that exhibits intrinsic ferromagnetism up to 360 K, accompanied by a strong perpendicular magnetic anisotropy (PMA) [18]. This development brings 2D magnetic materials into the room-temperature operation regime, opening up broad new opportunities for practical applications.

Naturally, tremendous efforts have been devoted to tuning the functional properties of $Fe_3GaTe_2$, among which chemical doping has emerged as the most promising approach. In

*Contact author: zclin@fjnu.edu.cn
†Contact author: jzcui@fudan.edu.cn

 ©2026 American Physical Society

particular, Ni doping has been demonstrated to offer a viable route to tailor the magnetic anisotropy of $Fe_3GaTe_2$, with the potential to realize full anisotropy control from out-of-plane to in-plane at high doping levels [19–22]. Since anisotropy determines the magnetocaloric performance of vdW magnets [23], Ni substitution provides an ideal platform to tune the anisotropic functional properties of $Fe_3GaTe_2$ for practical applications.

However, the microscopic mechanism of Ni doping in $Fe_3GaTe_2$ has long remained elusive. While Guo *et al*. found that Ni dopants preferentially occupy the vdW gap sites, the experimental observations have long been puzzling: Ten percent Ni intercalation only induces a minor contraction of the *c*-axis lattice parameter of less than 0.1 Å [22], which is in sharp contrast to the drastic contraction of nearly 0.5 Å reported by Chang *et al*. for a similar concentration of interstitial Fe atoms [24]. Recent studies have revealed that the real crystal structure of $Fe_3GaTe_2$ is not an ideal stoichiometric lattice but rather an intrinsically defective system with coexisting interstitial Fe atoms and Fe1 vacancies [24–27]. These native defects are not impurities, but the intrinsic structure of real $Fe_3GaTe_2$ samples: They are responsible for the room-temperature ferromagnetism of the material and can continuously tune $T_C$, spin disorder, and even topological spin textures such as room-temperature skyrmions [24,27]. However, most prior theoretical works have almost universally adopted the ideal stoichiometric lattice as the starting point, which largely neglected these intrinsic defects, leading to a persistent discrepancy between theoretical predictions and experimental observations: ideal-lattice models failed to reproduce the moderate structural and magnetic evolution observed in experiments, leaving the doping mechanism poorly understood.

Notably, this challenge is far from an isolated case in $Fe_3GaTe_2$ but rather a common, long-overlooked feature across the entire field of vdW materials. For instance, in the $Cr_xTe_y$ family of layered magnets, the content of interstitial Cr atoms can drastically tune the Curie temperature: The stoichiometric $Cr_5Te_8$ exhibits a $T_C$ of approximately 200 K [28], while the excess-intercalated $Cr_5Te_6$, with additional interstitial Cr atoms, can boost the $T_C$ up to around 340 K, enabling room-temperature ferromagnetism [29]. Similarly, in $Fe_3GeTe_2$, the Fe deficiency can lead to a wide variation of $T_C$ ranging from 150 K to 230 K, strongly dependent on the concentration of native Fe vacancies [16,30]. For $Fe_3GaTe_2$ itself, beyond tuning the $T_C$, the coexistence of interstitial Fe atoms and Fe vacancies can break the spatial inversion symmetry of the lattice, which further gives rise to topological spin order and even stabilizes room-temperature skyrmion states [27,31,32]. Notably, in the FeTe compound, the presence of interstitial Fe atoms led to a longstanding misinterpretation of its intrinsic ground state for decades: It was long mistakenly regarded as an intrinsic AFM metal, until recent studies revealed that the stoichiometric FeTe without interstitial defects is actually a superconductor with a critical temperature of 13.5 K [33]. These cases collectively highlight that 2D vdW materials often host non-negligible intrinsic defects, and conventional theoretical calculations based on idealized defect-free lattices can lead to substantial inaccuracies in predictions of the intrinsic physical properties of these materials.

Against this backdrop, we investigate Ni-doped $Fe_3GaTe_2$ using a realistic defective lattice model, aiming to resolve this persistent discrepancy. We systematically investigate the structural, magnetic, and magnetocaloric evolution upon Ni substitution and reveal an intrinsic defect-assisted doping mechanism that accounts well for all our experimental observations. This mechanism naturally explains the puzzling difference between Ni and Fe intercalation: Ni dopants preferentially substitute the preexisting interstitial Fe atoms rather than inserting into empty gaps, thus avoiding the drastic lattice contraction caused by new intercalation. It not only explains the moderate structural and magnetic evolution in our low-doping samples but also rationalizes the distinct property evolution reported in previous high-doping studies, unifying the seemingly scattered experimental results across different doping regimes. Our findings highlight the critical importance of incorporating intrinsic defects into theoretical models for vdW materials, paving the way for the rational design of advanced spintronic and magnetocaloric devices.

## II. METHODS

High-quality single crystals of Ni-doped $Fe_3GaTe_2$ were grown by the self-flux method [18]. Fe powders (3N, Aladdin), Ni powders (4N, Aladdin), Ga lumps (5N, Aladdin), and Te powders (4N, Aladdin) were mixed with a molar ratio of Fe:Ni:Ga:Te = 1-$x$:$x$:1:2 and sealed into an evacuated quartz tube. The actual Ni doping concentrations ($x$) in the grown crystals were determined to be 0%, 4.6%, 7.2%, and 8.5%, and the corresponding samples are labeled as Ni0, Ni4.6, Ni7.2, and Ni8.5, respectively. The mixture was first heated to 1273 K over 1 h and held at that temperature for 24 h to facilitate solid-state reactions. Subsequently, the temperature was rapidly decreased to 1153 K over 1 h, followed by a slow cooling process to 1053 K over 100 h. The Fe:Ni:Ga:Te ratio of the samples was measured using energy-dispersive x-ray spectroscopy (EDX), and homogeneous doping and elemental distribution were confirmed by EDX mapping. To further confirm the reliability of the lattice parameters, we performed additional powder x-ray diffraction (XRD) measurements on ground single crystal powders, which eliminated the preferred orientation effect. We then performed Rietveld refinement on the powder XRD patterns to obtain the full lattice parameters. The XRD patterns were measured at room temperature with Cu $K_\alpha$ radiation, and no impurities were observed. Magnetization measurements were performed using a Quantum Design Magnetic Property Measurement System (MPMS-7). The magnetocrystalline anisotropy energy (MAE) was derived from the magnetic anisotropy constant $K_u$, which was calculated via

$$K_u = \frac{H_k \cdot M_s}{2}. \quad (1)$$

where $H_k$ is the saturation field along the hard axis and $M_s$ is the saturation magnetization. This method is standard for characterizing uniaxial magnetic anisotropy in single crystals [34].

The first-principles calculations were performed using density functional theory as implemented in the Vienna *ab initio* Simulation Package [35,36]. The generalized gradient

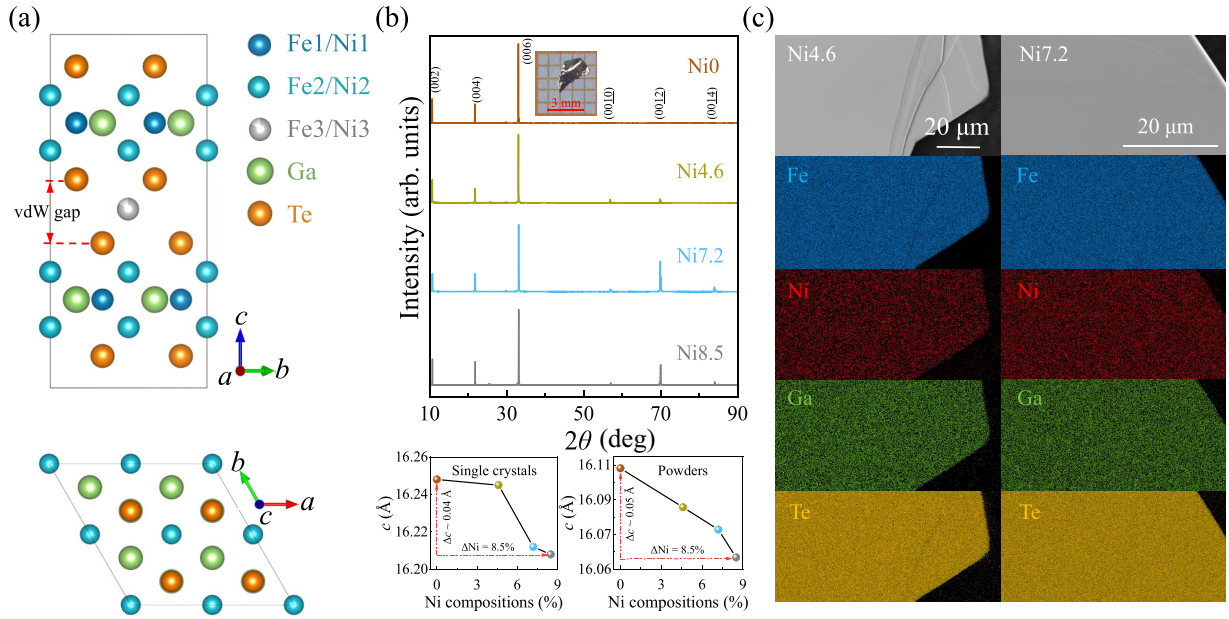


FIG. 1. Crystal structure and structural characterizations of Ni-doped $Fe_3GaTe_2$. (a) Schematic views of the crystal structure of Ni-doped $Fe_3GaTe_2$, depicting the atomic arrangement of Fe1, Fe2/Ni2, Ni3, Ga, and Te atoms, with the crystallographic axes and vdW gap indicated. (b) Top panel: XRD patterns for samples with varying Ni concentrations. The inset shows the optical image of the pristine Ni0 single crystal, with the (00$l$) diffraction peaks labeled in the patterns. Bottom panel: The corresponding out-of-plane lattice parameter $c$ as a function of Ni composition, for single crystalline (left) and powder (right) samples, respectively. A minor $c$-axis contraction of ∼0.04 Å and ∼0.05 Å is observed across the 8.5% Ni doping range for the two types of samples, respectively. (c) SEM morphology (top) and corresponding EDX elemental mapping (bottom) of Ni4.6 and Ni7.2 samples, demonstrating the uniform distribution of Fe, Ni, Ga, and Te atoms.

approximation (GGA) of the Perdew-Burke-Ernzerhof (PBE) [37] form was used for the exchange-correlation functional, and we adopted the DFT-D2 approach to account for the interlayer vdW interactions. The projector augmented-wave method [38] with a 550-eV plane-wave cutoff was employed. Different from most previous works which used the ideal stoichiometric lattice, we constructed our model based on the realistic defective lattice with coexisting interstitial Fe and Fe1 vacancies, which is the real structure of $Fe_3GaTe_2$ [24–27]. The in-plane lattice parameters and atomic positions were fully optimized until forces on each atom were less than $10^{-2}$ eV/Å. During the electronic self-consistent steps, the energy convergence criterion was set to $10^{-6}$ eV. The MAE was defined as $E_{MAE} = E_{[010]} - E_{[001]}$, where $E_{[010]}$ and $E_{[001]}$ represent the calculated energies with in-plane [010] and out-of-plane [001] magnetization directions, respectively. A positive $E_{MAE}$ implies an out-of-plane magnetic easy axis, while a negative value indicates an in-plane easy axis. To directly compare with experimental results, we converted the experimental MAE from J/m$^3$ to meV/f.u. using the calculated unit cell volume.

## III. RESULTS AND DISCUSSIONS

The crystal structure of Ni-doped $Fe_3GaTe_2$, as illustrated in Fig. 1(a), shows that Ni-doped $Fe_3GaTe_2$ crystallizes in a hexagonal structure (space group $P6_3/mmc$). In this layered vdW material, the vdW gap is located between adjacent Te-atom layers, and the lattice contains two distinct iron Wyckoff positions per layer, denoted as Fe1/Ni1 and Fe2/Ni2. Recent neutron diffraction studies have confirmed that the real crystal contains additional interstitial Fe atoms at the Fe3 site in the vdW gap, together with Fe1 vacancies, which form the intrinsic defect structure of $Fe_3GaTe_2$ [25]. Our theoretical calculations for undoped ideal lattice $Fe_3GaTe_2$ show the magnetic moments are 1.45 $\mu_B$ and 2.18 $\mu_B$ for the Fe1 and Fe2 sites, respectively, consistent with previous investigations [39–41]. We note that the local moments obtained from our calculations based on the GGA with PBE functional are slightly larger than those reported in prior studies based on the local density approximation (LDA). This trend follows the well-documented behavior of semilocal functionals for itinerant ferromagnets, where GGA systematically yields larger magnetic moments than LDA. Nevertheless, the total magnetic moment per formula unit from our calculation is in good agreement with both our experimental measurements and previous experimental reports. Detailed comparison of our ideal-structure calculation results with previous literature reports, including site-resolved magnetic moments and magnetic anisotropy energy, is provided in Table S1 of the Supplemental Material [42].

As shown in the upper panel of Fig. 1(b), the single-crystal XRD patterns only show the (00$l$) peaks, confirming the good orientation of the single crystal. The bottom panel of Fig. 1(b) summarizes the evolution of the out-of-plane lattice parameter $c$ as a function of Ni content, derived from XRD refinement for both single crystalline (left) and powder (right) samples. Across the full Ni doping range of 8.5%, both types of samples exhibit a consistent minor monotonic contraction of the $c$ axis: the single crystalline samples show a contraction of ∼0.04Å, with $c$ decreasing from 16.25 Å (Ni0) to 16.21 Å (Ni8.5), while the powder samples exhibit a slightly larger contraction

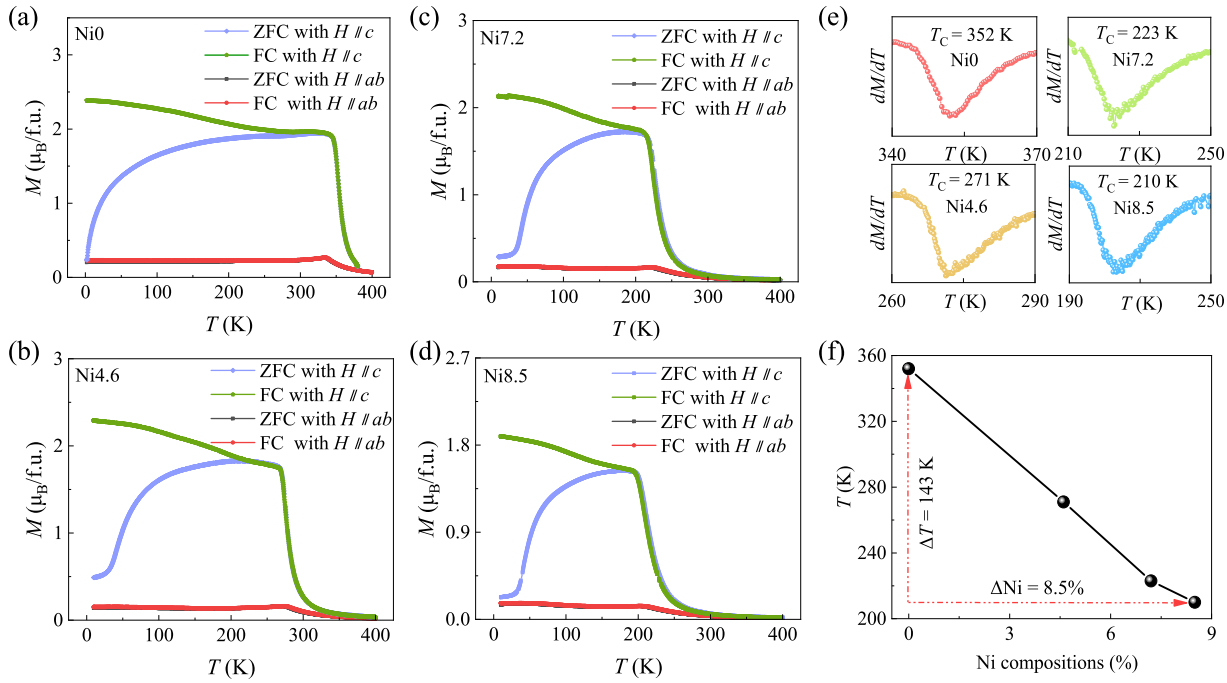


FIG. 2. Magnetic characterization of Ni-doped $Fe_3GaTe_2$ single crystals. [(a)–(d)] Temperature-dependent magnetization $M(T)$ measured at $H = 1000$ Oe for samples with Ni concentrations of 0%, 4.6%, 7.2%, and 8.5%, respectively, showing both ZFC and FC data along the in-plane (*ab* plane) and out-of-plane (*c*-axis) directions. (e) Temperature derivative of magnetization, $dM/dT$ versus temperature $T$, with minima determining the ferromagnetic $T_C$. (f) Evolution of $T_C$ as a function of Ni doping concentration $x$.

of ∼0.05Å, with $c$ decreasing from 16.11 Å (Ni0) to 16.06 Å (Ni8.5). This uniform lattice contraction along the $c$ axis further confirms the successful incorporation of Ni dopants into the host lattice. We also note that in the Ni-doped $Fe_3GaTe_2$ system studied by Guo *et al.*, the change of the $c$-axis parameter reaches nearly 0.085 Å at 10% Ni doping, which is noticeably larger than our observation [22]. We speculate that this difference originates from the Fe-deficient nature of their pristine $Fe_3GaTe_2$ samples, as evidenced by their slightly lower Curie temperature and weaker saturation magnetization compared to ours. This Fe deficiency is most likely derived from the lack of interstitial Fe atoms at the vdW gap. Specifically, their pristine sample has a larger $c$ parameter of 16.140 Å compared to our 16.113 Å, while their 10% Ni-doped sample has a $c$ parameter of ∼16.055 Å, which is very close to our 8.5% doped sample (16.061 Å). This indicates that the difference in lattice parameters mainly originates from the pristine samples, rather than the doping process itself, which explains the larger $c$-axis contraction during Ni doping in their system. Full details of the Rietveld refinement parameters for the powder XRD measurements, including the complete structural parameters and reliability factors, are summarized in Table S2 of the Supplemental Material [42]. Additionally, Fig. 1(c) presents the SEM morphology and corresponding EDX elemental mapping of the Ni4.6 and Ni7.2 samples. The uniform distribution of Fe, Ni, Ga, and Te elements across the entire mapping region confirms the homogeneous incorporation of Ni dopants into the host lattice, without any observable phase segregation.

The magnetic characterization of Ni-doped $Fe_3GaTe_2$, based on a series of magnetization measurements, was conducted under an applied field of 1000 Oe. Figures 2(a)–2(d) illustrate the temperature-dependent magnetization curves for samples with varying Ni concentrations, measured along both the in-plane ($H \parallel ab$) and out-of-plane ($H \parallel c$) under zero-field-cooled (ZFC) and field-cooled (FC) protocols. All $M(T)$ curves presented in the main text were measured after effective demagnetization of the sample. We note that without sufficient demagnetization, a small low-temperature negative magnetization can appear in the $H \parallel c$ ZFC curves as a measurement artifact, originating from the remanent magnetization preserved during the zero-field cooling process. This nonintrinsic artifact completely vanishes after full demagnetization, and the corresponding raw data with this artifact is provided in the Supplemental Material (Fig. S1) [42]. These curves reveal distinct ferromagnetic behaviors characterized by sharp phase transitions at $T_C$. Figure 2(e) depicts the determination of $T_C$ via the derivative of magnetization with respect to temperature, clearly showing a monotonic decrease in $T_C$ with increasing Ni doping. This is quantitatively summarized in Fig. 2(f), which plots $T_C$ versus Ni concentration, confirming a strong negative correlation.

The magnetic measurements of Ni-doped $Fe_3GaTe_2$ single crystals at 10 K reveal significant changes in magnetic properties with increasing Ni composition. Figures 3(a)–3(d) display the magnetization hysteresis loops, $M(H)$, for the four doping concentrations (0%, 4.6%, 7.2%, and 8.5%), measured with the magnetic field applied parallel to the $c$ axis ($H \parallel c$, red curves) and the *ab* plane ($H \parallel ab$, blue curves). The pristine sample (Ni0) exhibits clear ferromagnetic behavior with pronounced PMA, evidenced by the much larger saturation field along the *ab* plane, compared to the easy $c$ axis. From these hysteresis loops, we extract the key magnetic parameters summarized in Figs. 3(e) and 3(f). As shown in Fig. 3(e), the

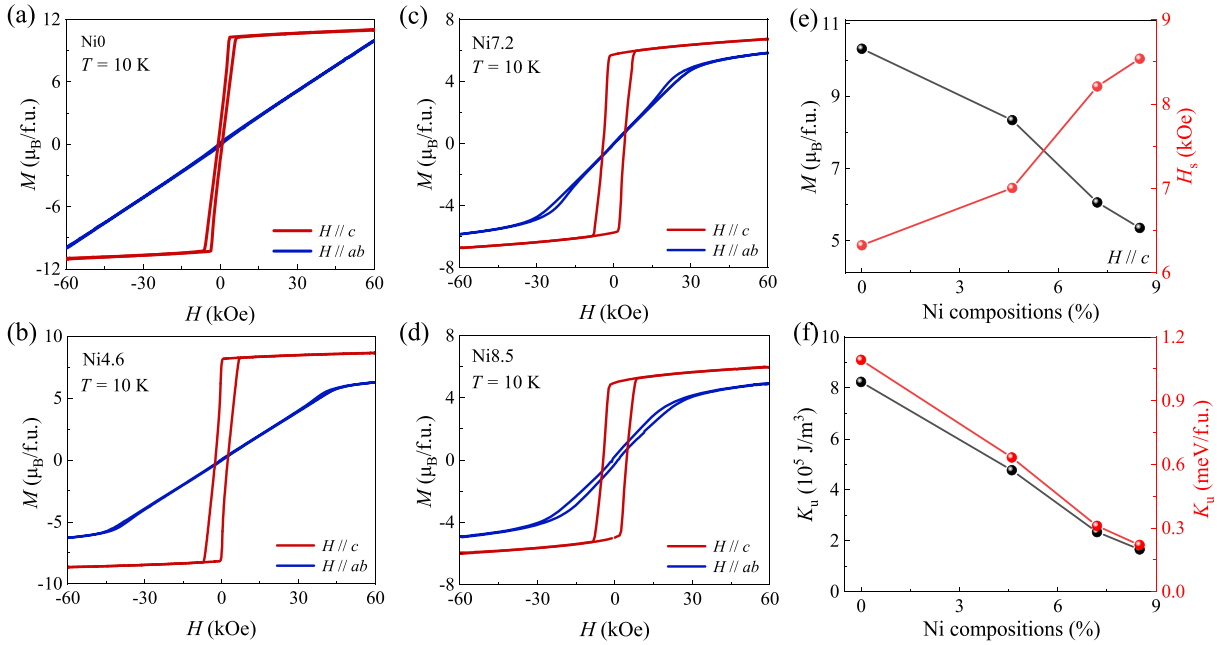


FIG. 3. Magnetic properties of Ni-doped $Fe_3GaTe_2$ at $T = 10$ K. [(a)–(d)] Magnetization hysteresis loops ($M(H)$ curves) for samples with Ni concentrations of 0%, 4.6%, 7.2% and 8.5%, measured with magnetic field applied parallel to the $c$ axis (red curves) and $ab$ plane (blue curves). (e) Saturation magnetization $M_s$ (black circles, left axis) and saturation field $H_s$ (red circles, right axis) vs Ni composition. (f) The magnetic anisotropy constant $K_u$ as a function of Ni composition, with the left axis in units of $10^5$ J/m$^3$ and the right axis in units of meV/f.u.

saturation magnetization $M_s$ decreases monotonically from 57.8 emu/g (Ni0) to 29.7 emu/g (Ni8.5). Conversely, the saturation field $H_s$ for $H \parallel c$ increases notably with doping concentration. The increased $H_s$ indicates changes in magnetic hardness and domain wall pinning. Figure 3(f) shows the magnetic anisotropy constant $K_u$ as a function of Ni doping, where $K_u$ decreases monotonically with Ni doping, clearly demonstrating that magnetic anisotropy can be effectively tuned by Ni doping. We also analyzed the evolution of coercivity $H_c$ with doping, and the detailed results and discussion are provided in the Supplemental Material (Fig. S2) [42]. More directly, the reduction of PMA by Ni doping closely mirrors that observed in Co- or Ni-doped $Fe_5GeTe_2$, where Co or Ni substitution for Fe is known to enhance in-plane magnetic anisotropy by altering the orbital occupancy and SOC strength [11,13]. These effects collectively weaken the ferromagnetic exchange interaction, leading to a gradual reduction of the magnetic ordering strength at higher doping levels.

All the experimentally derived structural and magnetic parameters for the four Ni-doped samples are summarized in Table I. Notably, these experimental values are in good qualitative agreement with our first-principles calculations based on the realistic defective lattice model, as summarized in Table III. For the pristine Ni0 sample, the experimental measurements yield an in-plane lattice parameter $a/b$ of 4.081 Å, out-of-plane parameter $c$ of 16.113 Å, total magnetic moment of 10.19 $\mu_B$/f.u., and ΔMAE of 1.20 meV/f.u. These values are consistent with our calculated results for the intrinsic defective configuration (Case 13 in Table III), where the corresponding theoretical values are $a/b = 3.975$ Å (half of the $2 \times 2 \times 1$ supercell in-plane size of 7.95 Å), $c = 15.78$ Å, total moment of 10.82 $\mu_B$/f.u., and ΔMAE of 1.64 meV/f.u. The small quantitative discrepancy can be naturally rationalized: First-principles calculations use a fixed defect concentration at a temperature of 0 K, while experiments are conducted at room temperature, and real crystals have slight native defect variations from flux growth. In addition, the inherent small numerical errors of first-principles methods also contribute to this minor difference.

TABLE I. The experimental results of crystal parameter, magnetization, and magnetic anisotropy energy for Ni0–Ni8.5.

| Composition | $a/b$ (Å) | $c$ (Å) | $M$ ($\mu_B$/f.u.) | ΔMAE (meV/f.u.) |
|---|---|---|---|---|
| Ni0 | 4.081 | 16.113 | 10.19 | 1.20 |
| Ni4.6 | 4.084 | 16.091 | 8.22 | 0.70 |
| Ni7.2 | 4.079 | 16.078 | 5.94 | 0.34 |
| Ni8.5 | 4.087 | 16.061 | 5.24 | 0.24 |

To elucidate the temperature evolution of magnetic properties, we conducted comprehensive initial isothermal magnetization measurements. As shown in Fig. 4, the isothermal magnetization curves, measured over the temperature range of 80 K to 400 K with 4 K intervals, for both field orientations ($H \parallel c$ and $H \parallel ab$) across all four doping concentrations, reveal the strong evolution of magnetic properties with both temperature and Ni composition. The host material $Fe_3GaTe_2$ exhibits strong PMA, where the magnetization preferentially aligns along the $c$ axis rather than the $ab$ plane; this anisotropic preference is significantly enhanced at low temperatures. A prominent feature of the undoped sample [Ni0, Fig. 4(b)] is the large separation and curvature of the magnetization isotherms measured along the $ab$ plane. Specifically, at high magnetic fields, the isotherms measured at lower temperatures lie below those measured at higher temperatures, creating

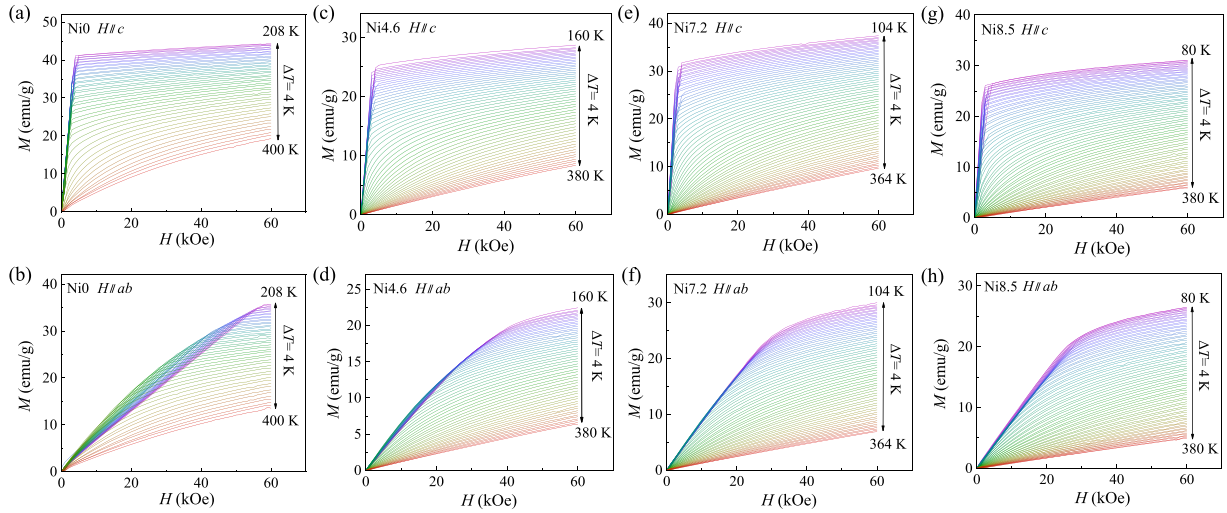


FIG. 4. Typical initial isothermal magnetization of Ni-doped $Fe_3GaTe_2$ single crystals. [(a)–(h)] Initial isothermal magnetization measured range within 80 to 400 K with 4 K intervals for different Ni concentrations (Ni0, Ni4.6, Ni7.2, and Ni8.5%) under two field orientations ($H \parallel c$ and $H \parallel ab$), showing the evolution of magnetic properties with temperature and doping concentration.

a characteristic "crossover" or "fanning-out" pattern that is completely absent in the $H \parallel c$ direction. This pattern is a well-known signature of strong PMA. This anomalous crossover behavior in the *ab* plane recovers to conventional ferromagnetic behavior at high temperatures, as the PMA weakens with increasing temperature. As the Ni concentration increases, these PMA-related features, namely the shrinking of the crossover region, progressively diminish: The effect is already weakened in Ni4.6, continues to fade in Ni7.2, and almost completely disappears in Ni8.5. The disappearance of the crossover effect, along with the recovery of conventional isothermal magnetization behavior, directly signals a substantial weakening of the PMA with increasing Ni doping, which provides direct experimental evidence for the effective tuning of magnetic anisotropy in $Fe_3GaTe_2$ via Ni substitution.

The magnetocaloric properties of Ni-doped $Fe_3GaTe_2$ also exhibit remarkable anisotropic behavior. The magnetic entropy change $-\Delta S_M$, a key parameter for evaluating magnetocaloric performance, was calculated from a series of isothermal magnetization curves using Maxwell's relation [43]:

$$\Delta S_M(T, \Delta H) = \int_0^{H_f} \left(\frac{\partial M}{\partial T}\right)_H dH. \tag{2}$$

Since the magnetization measurements were performed at small temperature intervals and discrete fields, $\Delta S_M(T_i, H)$ can be approximated as [44]

$$\Delta S_M(T_j, H) = \frac{\int_0^H M(T_j, H)dH - \int_0^H M(T_{j+1}, H)dH}{T_j - T_{j+1}}. \tag{3}$$

As shown in Figs. 5(a)–5(h), all measured samples exhibit characteristic peak-shaped $-\Delta S_M$ profiles, a definitive signature of a second-order magnetic phase transition, where the entropy change reaches its maximum near $T_C$. A key feature is the prominent crystalline anisotropy revealed by comparing the two field orientations. The strong PMA in the pristine sample (Ni0) leads to the crossover behavior in the magnetization isotherms [e.g., Fig. 4(b)], which further results in a region of negative magnetic entropy change in the corresponding *ab*-plane data [e.g., Fig. 5(b)]. In the Ni0 sample, we observe a notable anomaly, manifested as two distinct jump points, within the temperature range of 250–275 K, suggesting the possible occurrence of a phase transition. A recent study proposed that $Fe_3GaTe_2$ is best described as a self-intercalated ferrimagnet, where interstitial iron sites stabilize long-range magnetic order at high temperatures [25]. From this perspective, a first-order phase transition from a ferrimagnetic to a ferromagnetic state may occur in this temperature region, which accounts for the observed anomaly. A consistent trend is observed across all samples: For $H \parallel c$, we obtain significantly larger peak values of $-\Delta S_M$ compared to $H \parallel ab$. This indicates a substantially enhanced magnetocaloric response when the magnetic field is applied along the easy *c* axis, consistent with the fact that the field along the easy axis can more effectively align the spins, leading to a larger entropy change, as expected from the strong magnetic anisotropy of the system.

Figures 6(a) and 6(b) present the maximum magnetic entropy change $-\Delta S_M^{max}$ as a function of applied magnetic field for both field orientations ($H \parallel c$ and $H \parallel ab$) across all four Ni concentrations. The data demonstrate a characteristic field-dependent enhancement of $-\Delta S_M^{max}$, following the typical power-law relationship [61]:

$$-\Delta S_M^{max} \propto H^n. \tag{4}$$

The exponent *n* reflects the nature of the magnetic phase transition, with the peak value of $-\Delta S_M$ increasing systematically as the applied field rises from 5 to 60 kOe.

As shown in Fig. 6(c), which presents the relative cooling power (RCP) as a function of field for both orientations, we find that the RCP of all samples increases monotonically with increasing magnetic field. The RCP, a key parameter evaluating the cooling power of magnetocaloric materials, can be

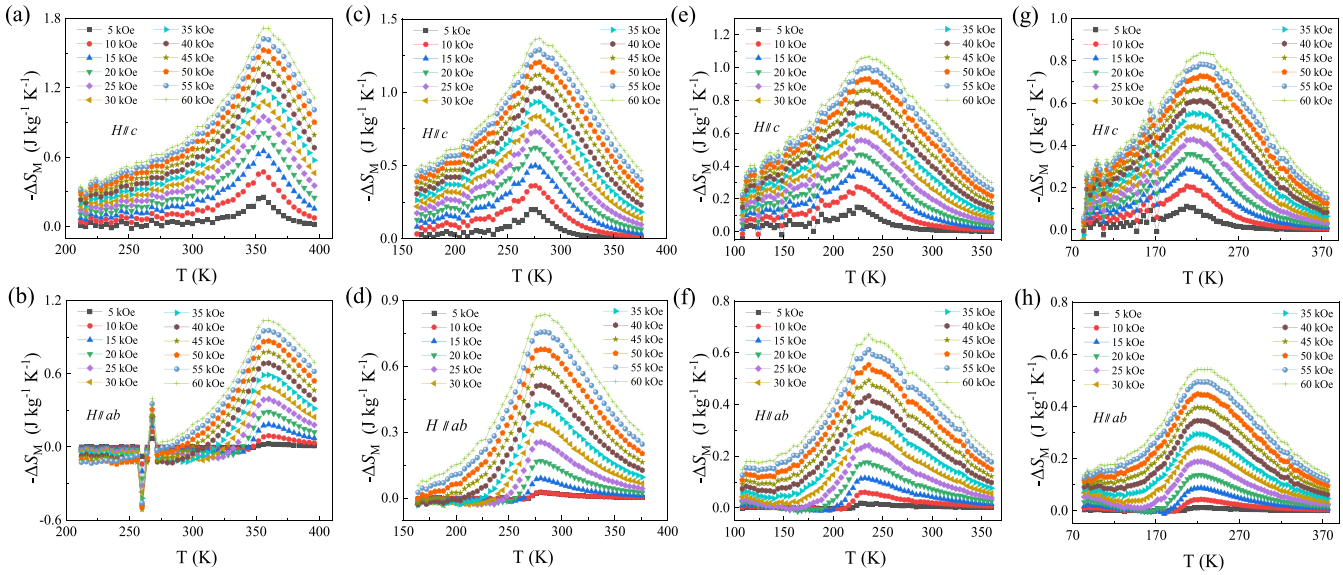


FIG. 5. Magnetic entropy change ($-\Delta S_M$) as a function of temperature for Ni-doped $Fe_3GaTe_2$ under various magnetic fields. Panels (a), (c), (e), and (g) correspond to $H \parallel c$ configuration; panels (b), (d), (f), and (h) represent $H \parallel ab$ orientation. Curves are measured at field strengths ranging from 5 to 60 kOe with 5-kOe increments.

calculated as

$$\mathrm{RCP} = -\Delta S_{\mathrm{M}}^{\max} \times \delta T_{\mathrm{FWHM}}, \tag{5}$$

where $\delta T_{\mathrm{FWHM}}$ is the full-width at half-maximum of the $-\Delta S_M(T)$ peak, which defines the effective working temperature range. Similarly, the RCP itself often exhibits a power-law dependence on the magnetic field, characterized by a critical exponent $m$,

$$\mathrm{RCP} \propto H^m. \tag{6}$$

Systematic analysis of Figs. 6(e)–6(g) reveals the key effects of Ni doping on the magnetocaloric properties of $Fe_3GaTe_2$, when benchmarked against other 2D vdW magnetic materials. Figure 6(e) demonstrates that $-\Delta S_{\mathrm{M}}^{\max}$ gradually decreases as $T_C$ is reduced from 352 K in the undoped Ni0 sample to 210 K in the Ni8.5 sample, while the performance remains highly competitive compared to other typical 2D magnets such as $Fe_3GeTe_2$ [30]. This controllable reduction of $T_C$ via Ni doping allows us to optimize the

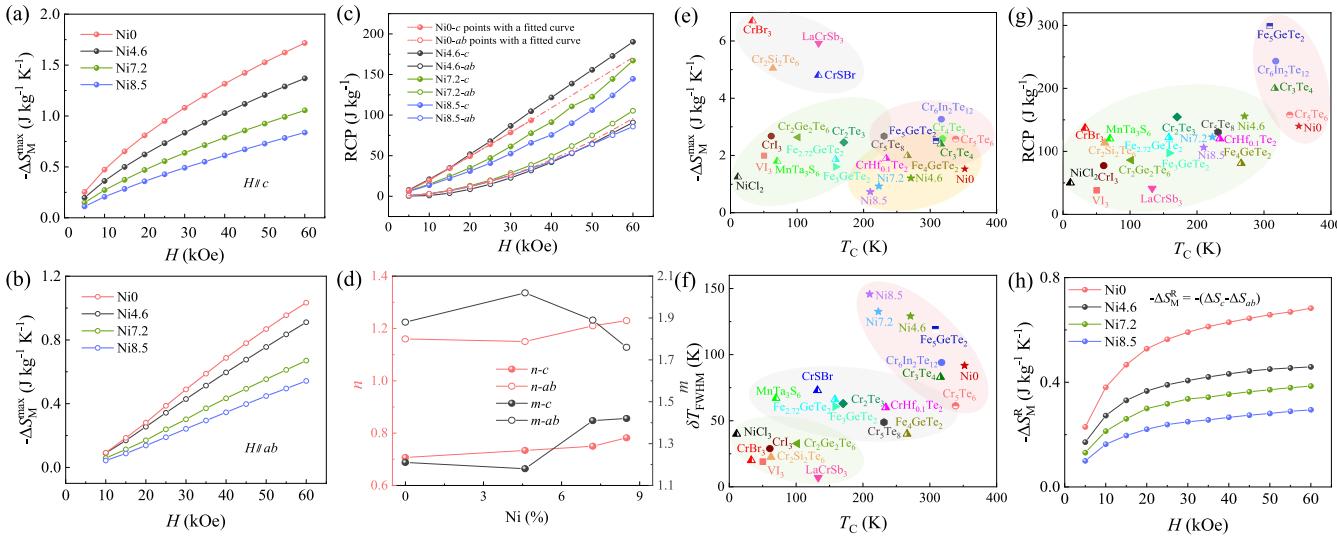


FIG. 6. Comprehensive analysis of magnetocaloric properties in Ni-doped $Fe_3GaTe_2$ and comparative study with typical 2D magnetic materials. [(a)–(c)] The maximum magnetic entropy change ($-\Delta S_{\mathrm{M}}^{\max}$) and relative cooling power (RCP) as a function of applied field for $H \parallel c$ and $H \parallel ab$ with varying Ni concentrations (Ni0, Ni4.6, Ni7.2, Ni8.5%). (d) The critical parameters $n$ and $m$ versus Ni composition for $H \parallel c$ and $H \parallel ab$. [(e)–(g)] Comparative analysis of $-\Delta S_{\mathrm{M}}^{\max}$, $\delta T_{\mathrm{FWHM}}$, and RCP with $T_C$. (h) The anisotropy analysis of magnetic entropy change. The data of (e), (f), and (g) are cited from $Fe_5GeTe_2$ [45], $Cr_2Te_3$ [46], $Fe_3GeTe_2$ [30], $Cr_5Te_8$ [47], $Cr_5Te_6$ [29], $CrI_3$ [48], $Cr_6In_2Te_{12}$ [49], $Cr_2Si_2Te_6$ [50], $Cr_2Ge_2Te_6$ [50], $LaCrSb_3$ [51], $CrBr_3$ [52], $Cr_3Te_4$ [53], CrSBr [54], $CrHf_{0.1}Te_2$ [55], $MnTa_3S_6$ [56],$Fe_{2.72}GeTe_2$ [57], $NiCl_2$ [58] $Fe_4GeTe_2$ [59], and $VI_3$ [60].

TABLE II. Comparison of $T_C$, $n$, $m$, $\delta T$, $-\Delta S_M^R$, and RCP for Ni-doped $Fe_3GaTe_2$ and various typical vdW ferromagnetic materials. $n$, $m$, and RCP collected from $H \parallel c$ data, and $-\Delta S_M^R$ and RCP from the data with $H = 50$ kOe.

| Composition | Reference | Method | $T_C$ (K) | $n$ | $m$ | $\delta T$ (K) | $-\Delta S_M^R$ (J kg$^{-1}$K$^{-1}$) | RCP (J kg$^{-1}$) |
|---|---|---|---|---|---|---|---|---|
| Ni0 | This work | MCE | 352 | 0.71 | 1.21 | 92 | 0.66 | 140 |
| Ni4.6 | This work | MCE | 271 | 0.73 | 1.18 | 129 | 0.45 | 156 |
| Ni7.2 | This work | MCE | 223 | 0.75 | 1.41 | 132 | 0.37 | 123 |
| Ni8.5 | This work | MCE | 210 | 0.78 | 1.42 | 146 | 0.28 | 106 |
| Theory | [62] | Mean-field | | 0.667 | 1.333 | | | |
| Theory | [63] | 3D-Heisenberg | | 0.637 | 1.208 | | | |
| Theory | [64] | 3D-XY | | 0.606 | 1.208 | | | |
| Theory | [63] | 3D-Ising | | 0.569 | 1.207 | | | |
| Theory | [65] | Tricritical mean-field | | 0.4 | 1.20 | | | |
| $Fe_{2.72}GaTe_2$ | [66] | MCE | 331 | ~0.65 | | | 0.7 | |
| $Fe_3GaTe_2$ | [67] | MCE | 341 | 0.69 | 1.3 | 107.8 | 0.56 | 180 |
| $Fe_3GeTe_2$ | [30] | MCE | 153 | 0.60 | 1.2 | 94 | 0.18 | 113 |
| $Fe_4GeTe_2$ | [59] | MCE | 266 | 0.68 | 1.21 | 40.7 | -0.04 | 81 |
| $Fe_5GeTe_2$ | [7] | MCE | 285 | 0.76 | 1.23 | 106 | -0.01 | 269 |
| $Cr_2Si_2Te_6$ | [50] | MCE | 32 | 0.52 | 1.12 | 22.6 | 0.29 | 114 |
| $CrBr_3$ | [52] | MCE | 33 | 0.63 | 1.03 | 20.5 | 0.17 | 137 |
| $CrI_3$ | [48] | MCE | 61 | 0.64 | 1.12 | 29 | 1.56 | 123 |

material for specific target temperature ranges. Concurrently, Fig. 6(f) shows a significant broadening of the magnetic phase transition, quantified by the increase of $\delta T_{FWHM}$ from ~91.73 K in Ni0 to 145.74 K in the Ni8.5 sample. This broadening correlates with the evolution of the critical exponents: The exponents of our pristine Ni0 sample are close to the theoretical values of the 3D-Heisenberg model, consistent with the nearly ideal ferromagnetic order in the undoped sample. With increasing Ni doping, the exponents gradually deviate from the ideal theoretical values: $n$ increases from 0.71 to 0.78, while $m$ increases from 1.21 to 1.42, confirming the enhanced magnetic disorder induced by Ni doping. Finally, Fig. 6(g) reveals that the RCP exhibits a nonmonotonic dependence on Ni doping, with the optimal cooling performance achieved at intermediate doping (Ni4.6). At this doping level, the increased $\delta T_{FWHM}$ partially compensates for the reduced $-\Delta S_M^{max}$, maximizing the practical cooling efficiency for targeted temperature regimes.

Figure 6(h) presents the anisotropy of the magnetic entropy change, defined as $-\Delta S_M^R = -(\Delta S_M^c - \Delta S_M^{ab})$. We find that this anisotropic entropy difference increases monotonically with magnetic field and gradually weakens with increasing Ni doping, directly demonstrating the suppression of PMA by Ni substitution.

All the key magnetocaloric parameters, including the critical exponents, transition temperature, and cooling performance, are systematically summarized in Table II, which provides a comprehensive benchmark of our Ni-doped $Fe_3GaTe_2$ against other typical vdW ferromagnetic materials.

Notably, we have specifically included the recent works of Hu *et al.* [67] and You *et al.* [66] in this comparison, which are the two recent works on the magnetocaloric properties of $Fe_3GaTe_2$ and its off-stoichiometric variants. For the pristine $Fe_3GaTe_2$ sample, Hu *et al.* reported a Curie temperature of 341 K, critical exponents of $n = 0.69$ and $m = 1.3$, and a maximum RCP of 180 J/kg. Our pristine Ni0 sample shows highly consistent results: Our $T_C$ of 352 K, $n = 0.71$ and $m = 1.21$ are in good quantitative agreement with their work, confirming the reliability of our experimental measurements. The minor quantitative difference can be well rationalized by the slight variation of intrinsic defect concentration: As discussed earlier, the native interstitial Fe concentration in real $Fe_3GaTe_2$ samples can continuously tune the Curie temperature and critical behavior, which explains the small deviation between different experimental groups. In terms of magnetocaloric performance, Hu *et al.*'s sample achieves a slightly higher RCP of 180 J/kg [67], which may be attributed to their higher intrinsic defect concentration that broadens the magnetic phase transition. Our Ni4.6 sample, with an optimal RCP of 156 J/kg, is already very close to this state-of-the-art value, while our intermediate doping level shifts the $T_C$ from 341 K to 271 K, bringing the working temperature much closer to room temperature, which is more suitable for practical solid-state cooling applications. For the off-stoichiometric $Fe_{2.72}GaTe_2$ sample, You *et al.* [66] reported a $T_C$ of 331 K and a critical exponent $n \approx 0.65$, which is consistent with the trend of Fe-deficient samples: Fe vacancies tend to reduce the critical exponent, bringing it closer to the mean-field theoretical value. In terms of magnetocaloric performance, our Ni4.6 sample achieves an optimal RCP of 156 J/kg at an intermediate doping level, which is highly competitive compared to other typical vdW ferromagnets: It outperforms many well-studied materials such as $Fe_3GeTe_2$ (113 J/kg), $Cr_2Si_2Te_6$ (114 J/kg), and $CrBr_3$ (137 J/kg) and is comparable to the state-of-the-art $Fe_3GaTe_2$ sample reported by Hu *et al.* [67]. This optimal performance at intermediate doping makes Ni-doped $Fe_3GaTe_2$ a promising candidate for room-temperature solid-state cooling applications, as it combines a Curie temperature of 271 K (close to room temperature) with a large cooling power and a broad working temperature range.

To clarify the microscopic doping mechanism underlying the experimentally observed structural and magnetic evolution in Ni-doped $Fe_3GaTe_2$, we performed systematic first-principles calculations. As-grown $Fe_3GaTe_2$ is

TABLE III. Theoretical calculations of Ni-doped $Fe_3GaTe_2$ compounds with various doping sites.[a]

| Composition | Case | $a/b$ (Å) | $c$ (Å) | ΔMAE (meV/f.u.) | Total $M$ ($\mu_B$/ f.u.) | Mean $M$ ($\mu_B$) |
|---|---|---|---|---|---|---|
| $Fe_{24}Ga_8Te_{16}$ | 1 | 8.00 | 16.14 | 2.89 | 11.1 | Fe1(1.45) Fe2(2.18) |
| $Fe_{23}NiGa_8Te_{16}$ | 2 | 8.00 | 16.13 | 4.67 | 11.02 | Fe1(1.45) Fe2(2.21) Ni1(0.25) |
| $Fe_{22}Ni_2Ga_8Te_{16}$ | 3 | 8.01 | 16.14 | 6.03 | 11 | Fe1(1.50) Fe2(2.26) Ni1(0.24) |
| $Fe_{23}NiGa_8Te_{16}$ | 4 | 7.99 | 16.15 | 2.5 | 10.63 | Fe1(1.46) Fe2(2.18) Ni2(0.14) |
| $Fe_{22}Ni_2Ga_8Te_{16}$ | 5 | 7.99 | 16.16 | 2.66 | 10.23 | Fe1(1.48) Fe2(2.12) Ni2(0.15) |
| $Fe_{23}NiGa_8Te_{16}$ | 6 | 7.94 | 15.88 | 0.29 | 10.24 | Fe1(1.48) Fe2(2.06) Ni3(-0.29) |
| $Fe_{22}Ni_2Ga_8Te_{16}$ | 7 | 7.89 | 15.79 | -0.8 | 9.4 | Fe1(1.53) Fe2(1.92) Ni3(-0.17) |
| $Fe_{23}Ni_2Ga_8Te_{16}$ | 8 | 7.99 | 15.96 | 0.08 | 10.62 | Fe1(1.49) Fe2(2.19) Ni2(0.12) Ni3(-0.36) |
| $Fe_{24}NiGa_8Te_{16}$ | 9 | 8.00 | 15.97 | 2.23 | 11.39 | Fe1(1.46) Fe2(2.29) Ni3(-0.48) |
| $Fe_{24}Ni_2Ga_8Te_{16}$ | 10 | 8.02 | 15.88 | 2 | 11.09 | Fe1(1.49) Fe2(2.20) Ni3(-0.36) |
| $Fe_{22}Ni_2Ga_8Te_{16}$ | 11 | 7.93 | 15.91 | 0.13 | 9.6 | Fe1(1.48) Fe2(2.02) Ni2(0.06) Ni3(-0.30) |
| $Fe_{23}NiGa_8Te_{16}$ | 12 | 7.89 | 15.72 | -1.12 | 9.83 | Fe1(1.56) Fe2(1.90) Fe3(1.68) Ni3(-0.19) |
| $Fe_{24}Ga_8Te_{16}$ | 13 | 7.95 | 15.78 | 1.64 | 10.82 | Fe1(1.46) Fe2(2.09) Fe3(1.76) |
| $Fe_{24}Ga_8Te_{16}$ | 14 | 7.90 | 15.61 | -1.09 | 10.24 | Fe1(1.59) Fe2(1.90) Fe3(1.54) |
| $Fe_{23}Ga_8Te_{16}$ | 15 | 7.94 | 16.01 | 0.38 | 10.2 | Fe1(1.46) Fe2(2.19) |
| $Fe_{22}Ga_8Te_{16}$ | 16 | 7.86 | 15.99 | -1.6 | 9.24 | Fe1(1.46) Fe2(1.89) |
| $Fe_{23}Ga_8Te_{16}$ | 17 | 7.97 | 16.10 | 1.72 | 10.29 | Fe1(1.48) Fe2(2.13) |
| $Fe_{22}Ga_8Te_{16}$ | 18 | 7.96 | 16.13 | 0.09 | 9.75 | Fe1(1.49) Fe2(2.11) |
| $Fe_{26}Ga_8Te_{16}$ | 19 | 8.05 | 15.73 | 2.13 | 12.16 | Fe1(1.53) Fe2(2.21) Fe3(1.51) |

[a]Doping sites:
(1) Ideal crystal lattice. (2) One Ni atom occupies Fe1 site. (3) Two Ni atoms occupy Fe1 site. (4) One Ni atom occupies Fe2 site. (5) Two Ni atoms occupy Fe2 site. (6) One Ni atom in Ni3 site and one Fe1 vacancy. (7) Two Ni atoms in Ni3 site and two Fe1 vacancies. (8) One Ni atom in Ni3 site and one in Fe2 site. (9) One Ni atom in Ni3 site. (10) Two Ni atoms in Ni3 site. (11) One Ni atom in Ni3 site and one Ni in Fe2 site with two Fe1 vacancies. (12) One Ni and one Fe in vdW site with two Fe1 vacancies. (13) One Fe atom in Fe3 site and one Fe1 vacancy. (14) Two Fe atoms in Fe3 site and two Fe1 vacancies. (15) One Fe1 vacancy. (16) Two Fe1 vacancies. (17) One Fe2 vacancy. (18) Two Fe2 vacancies. (19) Two Fe atoms in Fe3 site.

intrinsically defective, naturally hosting Fe1 vacancies and interstitial Fe atoms, while Ni dopants can potentially occupy multiple distinct lattice or interstitial sites and interact with these native defects. The microscopic occupation configuration of dopants, which directly governs the physical properties, is difficult to resolve experimentally. To disentangle the effect of different defect-dopant configurations, we constructed and calculated 19 distinct configurations, with the results summarized in Table III.

Cases 1–5, involving Ni substitution at the Fe1 and Fe2 host lattice sites, show that the in-plane lattice parameter $a/b$ remains largely unchanged around ∼8.00 Å, consistent with the minimal structural perturbation of Ni-for-Fe substitution to the in-plane Fe-Te framework. For Ni substitution at the Fe1 site (cases 2 and 3), the out-of-plane parameter $c$ remains almost identical to the ideal lattice (16.14 Å in case 1), as the internal substitution barely affects the interlayer vdW spacing. In contrast, substitution at the Fe2 site (cases 4 and 5) induces a slight increase of $c$, reaching up to 16.16 Å in case 5, due to the minor lattice relaxation of the outer-layer atom adjacent to the vdW gap. The ΔMAE exhibits a strong site-dependent response, which can be interpreted based on the microscopic origin of PMA in $Fe_3GaTe_2$ [68]. Notably, Ni substitution at the Fe1 (central) site significantly enhances ΔMAE: Case 3, with two Ni atoms substituting Fe1 sites, yields a large ΔMAE of 6.03 meV/f.u., more than double the ideal value of 2.89 meV/f.u. This enhancement arises from two factors: First, the effective SOC of Ni's $3d$ orbitals is much stronger than that of Fe, introducing an additional positive contribution to the magnetocrystalline anisotropy. Second, this substitution acts as weak electron doping, which further stabilizes the positive SOC contribution of Te $p_x/p_y$ orbitals—the core origin of PMA in this system [39]—without disrupting the critical Fe-Te orbital hybridization. Notably, our calculated MAE and total $M$ for the ideal lattice are in good agreement with the previously reported result of ∼2.64 meV/f.u. and ∼11.58 $\mu_B$/f.u. by Zhang *et al.* [69], where their calculations also adopted the GGA functional, validating the reliability of our computational setup. In contrast, substitution at the Fe2 site leads to a moderate reduction of ΔMAE to ∼2.6 meV/f.u. This is because the outer Fe2 site is the core contributor to PMA: The Fe2-Te hybridization is the basis for the positive Te $p_x/p_y$ SOC contribution [70]. Ni substitution here fills the unoccupied states of Te's $p$ orbitals, reducing the energy difference between occupied and unoccupied states that is essential for the Te SOC contribution, thus weakening the core source of PMA. Consistent with this trend, the total magnetic moment also shows site-dependent evolution: It gradually decreases with increasing Ni substitution at the Fe2 site, from 11.1 $\mu_B$/f.u. in the ideal case to 10.23 $\mu_B$/f.u. in case 5, as the high-moment outer Fe2 is replaced by lower-moment Ni. In contrast, Ni substitution at the Fe1 site preserves a high total magnetic moment of ∼11 $\mu_B$/f.u., since the central Fe1 has a lower intrinsic moment, and its substitution barely affects the large moments of outer Fe2 and Te atoms. Furthermore, our calculation confirms that Fe1 vacancy (case 15) drastically reduces ΔMAE to 0.38 meV/f.u., which is attributed to the hole-doping effect of Fe vacancies

that weakens the Te $p_x/p_y$ SOC contribution, explaining the PMA suppression in Fe-deficient $Fe_3GaTe_2$ samples [39].

Next, we investigated configurations where Ni atoms are incorporated into the vdW gap site (Ni3). For cases 6 and 7, where interstitial Ni doping is accompanied by Fe1 vacancies, we observe a notable contraction of the *c*-axis lattice parameter, which decreases to 15.88 Å in case 6 and 15.79 Å in case 7, indicating significant interlayer compression induced by the additional interstitial dopants. Correspondingly, the magnetic anisotropy is largely suppressed: ΔMAE drops to 0.29 meV/f.u. in case 6 and becomes negative (–0.8 meV/f.u.) in case 7, suggesting a spin reorientation from the *c*-axis easy direction to the *ab*-plane easy plane. The total magnetic moment is also notably reduced to 10.24 $\mu_B$/f.u. and 9.4 $\mu_B$/f.u., respectively. This rapid suppression of the total magnetic moment originates from the antiferromagnetic coupling of the interstitial Ni atoms: Quantitatively, each interstitial Ni atom introduces a net reduction of 3.6 $\mu_B$ to the total magnetic moment of the system. This value is in good agreement with the previously reported value of 4.1 $\mu_B$ per interstitial Ni atom by Guo *et al*. [22], where the minor quantitative difference can be well rationalized by the different exchange-correlation functionals adopted in the calculations: Their work employed the LDA functional, while our calculations are based on the GGA functional, which is known to introduce a small systematic deviation in the calculated magnetic moments for this class of vdW magnetic systems. For Ni atoms solely occupying the vdW gap site without accompanying Fe vacancies (cases 9 and 10), the lattice parameters show moderate change, with $a/b$ remaining around 8.00–8.02 Å and *c* moderately reduced to 15.97–15.88 Å. The ΔMAE values are moderately lower than the ideal case, reaching 2.23 meV/f.u. and 2.0 meV/f.u. for single and double Ni interstitial doping, respectively. Notably, the interstitial Ni atoms at the Ni3 site carry a clear negative atomic moment, confirming their antiferromagnetic alignment with the Fe host sublattice. We find that Ni atoms located at the vdW gap site have the strongest negative effect on the ferromagnetic order: They not only reduce the total magnetic moment but also introduce antiferromagnetic coupling that disrupts the long-range ferromagnetic order of the host system, which may naturally account for the drastic suppression of both the saturation magnetization and the Curie temperature even at low Ni doping concentrations [19–22].

Importantly, configurations where Fe atoms occupy the vdW gap site accompanied by Fe1 vacancies (cases 13 and 14) represent the typical intrinsic defective states of $Fe_3GaTe_2$ with different defect concentrations. As widely reported, the as-grown $Fe_3GaTe_2$ crystals are not ideal pristine lattices but naturally contain Fe1 vacancies and interstitial Fe atoms located at the vdW gap. In contrast, case 14 corresponds to a much higher intrinsic defect concentration (two interstitial Fe atoms and two Fe1 vacancies), which would induce a larger *c*-axis contraction and even invert the sign of MAE to –1.09 meV/f.u. Notably, Fe1 vacancies play a crucial role in tuning the magnetic anisotropy. In reality, bulk crystals are unlikely to host such a high concentration of Fe1 vacancies. Studies have reported that the occupancy rate of the Fe1 site is approximately 90% [25], which implies an Fe vacancy concentration of 3.3%, far below the 8.33% vacancy concentration in the high-defect case 14 (two Fe1 vacancies in our 24-Fe supercell), explaining why the in-plane easy axis (inverted MAE sign) is never observed in actual samples. Furthermore, when excess Fe atoms are introduced into the system, we obtain case 19, where two new Fe atoms are inserted into the empty vdW gap sites, leading to a Fe/Ga ratio of 3.25, close to the $Fe_{3.3}GaTe_2$ composition reported by Chang *et al.* [24]. Experimentally, their excess-Fe-intercalated $Fe_{3.3}GaTe_2$ samples exhibit significantly enhanced saturation magnetization, as well as a high Curie temperature approaching 380 K. Our calculations further reveal that the introduction of interstitial Fe atoms gives rise to a noticeable increase of the local atomic magnetic moments of the neighboring Fe1 and Fe2 host atoms, and the enhanced ferromagnetic exchange interactions thereby account for the observed enhancement of the macroscopic magnetic properties. This configuration induces a large *c*-axis contraction to 15.73 Å, accompanied by a substantial enhancement of the total magnetic moment to 12.16 $\mu_B$/f.u., which is close to the experimental observations of Chang *et al*. Specifically, their excess Fe-intercalated $Fe_{3.3}GaTe_2$ exhibits a (002) XRD peak shifted to ∼11.3° (compared to ∼11.0° in their pristine $Fe_3GaTe_2$). Based on Bragg's law, this peak shift corresponds to a drastic contraction of the out-of-plane lattice parameter, from 16.12 Å in their pristine sample to 15.66 Å in the Fe-rich sample, which matches our calculated *c* parameter of 15.73 Å for case 19 very well, considering the small numerical error in DFT calculations and the actual samples with defects. This confirms that only the introduction of new interstitial atoms would induce such a large structural change and magnetic moment enhancement, which is not the case in our Ni-doped samples.

After Ni substitution, the combined effect of Fe1 vacancies and the antiferromagnetic coupling of the interstitial Ni atoms leads to the gradual reduction of MAE with increasing Ni concentration: The experimental ΔMAE decreases from 1.20 meV/f.u. in Ni0 to 0.24 meV/f.u. in Ni8.5, corresponding to an 80% reduction, which is well reproduced by our theoretical calculations. Crucially, this process still maintains the positive ΔMAE throughout the doping range, which preserves the *c*-axis easy magnetic direction, consistent with the experimental observation that Ni-doped samples always maintain the out-of-plane magnetic anisotropy. Meanwhile, the total magnetic moment also decreases gradually from 10.19 $\mu_B$/f.u. to 5.24 $\mu_B$/f.u. with increasing Ni doping, consistent with the theoretical trend of moment reduction induced by the antiferromagnetic coupling of interstitial Ni atoms.

We then isolated the effect of intrinsic Fe vacancies by investigating cases 15–18. All vacancy-containing systems exhibit *c*-axis contraction, with the double Fe1 vacancy case (Case 16) showing the largest contraction to 15.99 Å, while Fe2 vacancies (case 17) induce only a minor contraction to 16.10 Å. The MAE of these systems varies strongly with vacancy site and concentration, ranging from –1.6 to 1.72 meV/f.u., confirming that Fe vacancies are strong regulators of magnetic anisotropy: High Fe1 vacancy concentrations would drive the system to an in-plane easy axis, which is inconsistent with our experimental observation of persistent out-of-plane anisotropy. The total magnetic moment decreases systematically with increasing vacancy concentration, as

expected from the removal of magnetic Fe atoms from the ferromagnetic host.

We further explored mixed doping configurations combining substitutional doping, interstitial doping and vacancies: Case 8 (one interstitial Ni plus one Fe2-substituted Ni) shows a slight $c$-axis contraction to 15.96 Å, a near-zero ΔMAE of 0.08 meV/f.u., and a slightly reduced total moment of 10.62 $\mu_B$/f.u.; case 12 (intercalated Ni/Fe plus two Fe1 vacancies) induces a larger $c$-axis contraction to 15.72 Å, a negative MAE of –1.12 meV/f.u., and a total moment of 9.83 $\mu_B$/f.u.; while case 11 (interstitial Ni, Fe2-substituted Ni, plus two Fe1 vacancies) yields a 15.91 Å $c$ parameter and a reduced total moment of 9.6 $\mu_B$/f.u.

Overall, Table III provides a comprehensive design map for tuning spin-orbit-coupling-mediated magnetic anisotropy, where specific combinations of defects and dopants allow precise control of the MAE, lattice parameters, and magnetization. Our results support a defect-assisted occupation model for Ni-doped $Fe_3GaTe_2$: As established in previous studies, the as-grown host material is not an ideal stoichiometric lattice but is intrinsically defective, naturally hosting a low concentration of preexisting Fe1 vacancies and interstitial Fe atoms within the vdW gap [25,26]. Notably, the presence of these interstitial Fe atoms can drastically reduce the out-of-plane lattice constant $c$, as previously reported by Chang *et al.* [24]. Consistent with the sequential doping model proposed by Guo *et al.*, which suggests that Ni dopants with lower concentrations preferentially occupy the vdW gap sites rather than substituting host lattice sites [22], we find that upon doping, Ni atoms preferentially substitute these preexisting interstitial Fe atoms, with only a small fraction of dopants inserting into the empty interlayer space. Notably, our calculations reveal that interstitial Fe atoms induce a stronger interlayer compression than interstitial Ni atoms under the same defect concentration: For the single-interstitial case, the Fe-intercalated configuration (case 13) yields a $c$ parameter of 15.78 Å, while the Ni-intercalated configuration (case 6) gives a slightly larger $c$ of 15.88 Å. This indicates that a pure 1:1 substitution of preexisting interstitial Fe by Ni would naturally lead to a slight expansion of the interlayer distance. However, our experimental observation shows a minor contraction of the $c$ axis, which strongly suggests that a small fraction of Ni dopants additionally insert into the empty interlayer sites, introducing a minor interlayer compression that compensates the expansion effect and results in the net small contraction observed experimentally. For the majority of dopants, this substitution mechanism only replaces the atomic species at the interstitial site without changing the total number of intercalated atoms, while the small fraction of new intercalated atoms only induces a minor interlayer compression. As a result, the interlayer distance shows only a minor contraction after doping, which accounts well for our experimental structural evolution: The in-plane lattice parameter $a/b$ remains nearly unchanged, evolving only slightly from 4.081 Å in Ni0 to 4.087 Å in Ni8.5, while the out-of-plane parameter $c$ decreases by only 0.052 Å, from 16.113 Å to 16.061 Å. In sharp contrast, the conventional interstitial doping model, where Ni atoms are additionally inserted into empty vdW gaps (exemplified by case 7), would induce a significant $c$-axis contraction of 0.35 Å relative to the ideal lattice, which is in clear contradiction to the moderate structural evolution observed in our experiments. This mechanism well reproduces all the measured structural and magnetic evolution across the full Ni doping range, in clear contrast to conventional single-site doping models that fail to explain the experimental observations. This tuning capability offers a viable route to tailor the physical properties of Ni-doped $Fe_3GaTe_2$ for spintronic applications.

Specifically, Ni doping induces a decrease in $T_C$ and weakening of ferromagnetism in $Fe_3GaTe_2$. The microscopic origin of this effect is clarified by the calculation results in our Supplemental Material [42]. For the spin-resolved band structures (Figs. S3 and S4) [42], Ni incorporation modifies the electronic states near the Fermi level ($E_F$): With Ni substituting the preexisting interstitial Fe atoms, the strong spin splitting between majority- and minority-spin bands near $E_F$ is gradually suppressed, leading to the weakening of spin asymmetry during doping. For the projected density of states (PDOS) (Figs. S5–S7) [42], the strong asymmetry between spin-up and spin-down states near $E_F$ in the pristine sample, which originates from the interstitial Fe3 atoms and the host Fe1/Fe2 atoms, corresponds to the high spin polarization of undoped $Fe_3GaTe_2$ (Ni0). In contrast, after Ni substitution, the interstitial Ni3 atoms introduce new electronic states at the interstitial site, which significantly reduces the overall spin asymmetry of the total DOS near $E_F$, directly resulting in decreased spin polarization and weakened ferromagnetism. The PDOS analysis further confirms that the electronic states of the host Fe1, Fe2, Ga, and Te atoms are barely affected by Ni doping, with only the interstitial site's states being modified. This validates that Ni dopants preferentially substitute the preexisting interstitial Fe sites, rather than the host lattice sites, which consistently accounts for the moderate structural and magnetic evolution observed in our experiment. In summary, Ni doping regulates the electronic states at the interstitial site, alters the composition of spin-asymmetric states at $E_F$ and ultimately modulates the electronic spin structure of $Fe_3GaTe_2$ while weakening its spin polarization. This conclusion is consistent with the results reported in previous studies [22].

Our work, combined with recent scattered observations in other vdW magnetic systems, suggests that intrinsic native defects could be the core origin of the persistent ideal-lattice discrepancy that has been observed across the community. Moving forward, we propose that future studies should consider establishing a defect-aware research paradigm, rather than continuing to rely solely on the idealized defect-free lattice model, which could pave the way for resolving the persistent experimental inconsistencies and advancing the entire field.

## IV. CONCLUSIONS

Two-dimensional vdW ferromagnets have emerged as a promising platform for next-generation spintronic and solid-state cooling technologies, yet the microscopic mechanism of chemical doping in these materials has long remained elusive, plagued by the persistent discrepancy between ideal-lattice theoretical predictions and experimental observations. In this work, we address this persistent challenge by investigating Ni-doped $Fe_3GaTe_2$, a prototypical room-temperature vdW

ferromagnet, using a realistic defective lattice model that explicitly incorporates the native interstitial Fe atoms and Fe1 vacancies, which are now confirmed as the intrinsic crystal structure of real $Fe_3GaTe_2$ samples [24–27].

We reveal an intrinsic defect-assisted occupation mechanism for Ni dopants: Rather than inserting into empty vdW gaps as conventional interstitial doping models assumed, most Ni atoms preferentially substitute the preexisting interstitial Fe sites. This mechanism naturally accounts for all our experimental observations: the moderate $c$-axis contraction of $\sim$0.05Å, the $\sim$80% reduction of MAE with the out-of-plane easy axis preserved, as well as the monotonic decrease of Curie temperature $T_C$ and total magnetic moment. Systematic magnetocaloric analysis further demonstrates that Ni doping effectively tunes the anisotropic functional properties: It suppresses the anisotropy of the magnetic entropy change ($-\Delta S_M^R$), broadens the magnetic phase transition width $\delta T_{FWHM}$, and yields an optimal RCP of 156 J/kg at an intermediate Ni concentration of 4.6%, which is well suited for room-temperature solid-state cooling applications.

Notably, our defect-aware model reconciles the apparent discrepancy between ideal-lattice predictions and experimental observations across the full doping range. It not only reproduces our low-doping experimental measurements with good agreement but also consistently explains the distinct property evolution reported in previous high-doping Fe self-intercalation studies [24]: When the doping concentration exceeds the intrinsic interstitial Fe concentration, the preexisting interstitial sites become saturated, and excess dopants begin to insert into the empty vdW gaps. This transition of the occupation mechanism naturally gives rise to the large lattice contraction observed in high-doping regimes, rationalizing the distinct property evolution observed across different doping concentrations.

This work elucidates the structure-property relationship for anisotropy engineering in 2D magnets and demonstrates that defect-assisted doping can serve as a precise, effective knob to tailor the functional properties of vdW ferromagnets. Beyond Ni-doped $Fe_3GaTe_2$, our findings highlight the importance of incorporating intrinsic defects into theoretical models for vdW materials, which provides important insights for the rational design of advanced spintronic and magnetocaloric devices tailored for practical applications.

## ACKNOWLEDGMENTS

This work is supported by the National Key Technologies R and D Program of China (Grants No. 2022YFA1404700 and No. 2022YFA1207000), National Natural Science Foundation of China (Grants No. 52101214, No. 62375054, and No. 62474041), Shanghai Rising-Star Program (Grant No. 24QA2700700), Science and Technology Commission of Shanghai Municipality (Grants No. 24520750200 and No. 24CL2900200), Shanghai Talent Programs, and the Natural Science Foundation of Fujian Province (Grant No. 2025J01657). The authors thank the assistance of the State Key Laboratory of Surface Physics at Fudan University for providing the experimental facilities (MPMS) and technical support.

## DATA AVAILABILITY

The data that support the findings of this article are not publicly available because they are owned by a third party and the terms of use prevent public distribution. The data are available from the authors upon reasonable request.

[1] N. D. Mermin and H. Wagner, Absence of ferromagnetism or antiferromagnetism in one-or two-dimensional isotropic Heisenberg models, Phys. Rev. Lett. **17**, 1133 (1966).

[2] S. Zhao, Z. Zhou, B. Peng, M. Zhu, M. Feng, Q. Yang, Y. Yan, W. Ren, Z.-G. Ye, Y. Liu, and M. Liu, Quantitative determination on ionic-liquid-gating control of interfacial magnetism, Adv. Mater. **29**, 1606478 (2017).

[3] X. Zhou, I. A. Malik, R. Duan, H. Shi, C. Liu, Y. Luo, Y. Sun, R. Chen, Y. Liu, S. Xia, V. L. Zhang, S. Liu, C. Zhu, X. Zhang, and Y. Du, Strain-induced robust skyrmion lattice at room temperature in a van der Waals ferromagnet, Adv. Mater. **37**, 2505977 (2025).

[4] Y. Hou and R. Wu, Magnetic anisotropy in 2D van der Waals magnetic materials and their heterostructures: Importance, mechanisms, and opportunities, Adv. Funct. Mater. **35**, e09453 (2025).

[5] Y. Zhao, H.-B. Yu, C.-Y. Zhao, D.-N. Kong, D.-N. Wang, L.-Y. Fu, Q.-M. Hu, D. Li, T.-Y. Zang, S.-J. Zheng, Y. Zhou, and J.-D. Zhou, Anisotropy and synaptic plasticity in CrSBr/$WSe_2$ heterojunction for advanced neural network applications, Rare Met. **44**, 6483 (2025).

[6] X. Zhou, Y. Shang, T. Luo, Y. Peng, and H. Fu, Large rotating magnetocaloric effect of textured polycrystalline $HoB_2$ alloy, Appl. Phys. Lett. **120**, 132401 (2022).

[7] R. Liang, L. Zhou, J. Liu, and N. Tang, Anisotropic magnetic critical behavior of van der Waals room-temperature ferromagnet $Fe_5GeTe_2$, J. Appl. Phys. **136**, 193902 (2024).

[8] J. Y. Moon, M. K. Kim, Y. J. Choi, and N. Lee, Giant anisotropic magnetocaloric effect in double-perovskite $Gd_2CoMnO_6$, Sci. Rep. **7**, 16099 (2017).

[9] Y. Gong, X.-F. Miao, T. Samanta, C. Taake, J. Liu, F.-J. Qian, Y.-Y. Shao, Y.-J. Zhang, Q.-Y. Ren, L. Caron, and F. Xu, Anomalous thermal expansion and enhanced magnetocaloric effect in <001>-textured $Mn_xFe_{5-x}Si_3$ alloys, Rare Met. **43**, 2263 (2024).

[10] G. Zhang, H. Wu, L. Yang, Z. Chen, W. Jin, B. Xiao, W. Zhang, C. Song, and H. Chang, Above-room-temperature ferromagnetism regulation in two-dimensional heterostructures, J. Am. Chem. Soc. **146**, 34070 (2024).

[11] J. Zhang, Z. Wang, Y. Xing, X. Luo, Z. Wang, G. Wang, A. Shen, H. Ye, S. Dong, and L. Li, Enhanced magnetic and

electrical properties of Co-doped $Fe_3GeTe_2$, Appl. Phys. Lett. **124**, 103103 (2024).

[12] L.-F. Wang, K.-B. Wang, Q.-M. Chen, C. Wu, X.-H. Wang, and M. Yan, Tuned bi-anisotropy of $Y_2Co_{14}B$ nanocrystalline magnetic alloys toward high-frequency applications, Rare Met. **44**, 1243 (2025).

[13] X. Hu, D.-X. Yao, and K. Cao, Tuning magnetic anisotropy in a $Fe_5GeTe_2$ monolayer through doping and strain, Phys. Rev. B **110**, 184418 (2024).

[14] B. Huang, G. Clark, E. Navarro-Moratalla, D. R. Klein, R. Cheng, K. L. Seyler, D. Zhong, E. Schmidgall, M. A. McGuire, P. Jarillo-Herrero, and X. Xu, Layer-dependent ferromagnetism in a van der Waals crystal down to the monolayer limit, Nature (London) **546**, 270 (2017).

[15] S. Jiang, L. Li, Z. Wang, K. F. Mak, and J. Shan, Controlling magnetism in 2D $CrI_3$ by electrostatic doping, Nat. Nanotechnol. **13**, 549 (2018).

[16] Y. Deng, Y. Yu, Y. Song, J. Zhang, N. Z. Wang, Z. Sun, Y. Yi, Y. Z. Wu, S. Wu, J. Zhu, J. Wang, X. H. Chen, and Y. Zhang, Gate-tunable room-temperature ferromagnetism in two-dimensional $Fe_3GeTe_2$, Nature (London) **563**, 94 (2018).

[17] G. Zhang, F. Guo, H. Wu, X. Wen, L. Yang, W. Jin, W. Zhang, and H. Chang, Above-room-temperature strong intrinsic ferromagnetism in 2D van der Waals $Fe_3GaTe_2$, Nat. Commun. **13**, 5067 (2022).

[18] S. Wu, Z. He, M. Gu, L. Ren, J. Li, B. Deng, D. Wang, X. Guo, W. Li, M. Chen, Y. Chen, M. Meng, Q. Ye, B. Shen, X. Chen, J. Guo, G. Xing, I. K. Sou, and S. Li, Robust ferromagnetism in wafer-scale $Fe_3GaTe_2$ above room-temperature, Nat. Commun. **15**, 10765 (2024).

[19] K.-H. Son, S. Oh, J. Lee, S. Yun, Y. Shin, S. Yan, C. Jang, H.-S. Lee, H. Lei, S. Y. Park, and H. Ryu, Persistent ferromagnetic ground state in pristine and Ni-doped $Fe_3GaTe_2$ flakes, Nano Converg. **11**, 55 (2024).

[20] H.-B. Ahn, S.-G. Jung, H. Lim, K. Kim, S. Kim, T.-E. Park, T. Park, and C. Lee, Giant coercivity enhancement in a room-temperature van der Waals magnet through substitutional metal-doping, Nanoscale **15**, 11290 (2023).

[21] K. Zhu, M. Wang, Y. Deng, M. Tian, B. Lei, and X. Chen, Effect of Co or Ni substitution on magnetism in the layered van der Waals ferromagnet $Fe_3GaTe_2$, Phys. Rev. B **109**, 104402 (2024).

[22] J. Yuan, H. Wang, X. Hou, B. Zhang, Y. Wei, J. Guo, L. Sun, Z. Yu, X. Liu, W. Xia, X. Wang, X. Liu, Y. Chen, S. Zhang, X. Fu, K. Qu, Z. Yang, and Y. Guo, Direct visualization of the impurity occupancy road map in Ni-substituted van der Waals ferromagnet $Fe_3GaTe_2$, Nano Lett. **25**, 4260 (2025).

[23] H. B. Tran, H. Momida, Y. Matsushita, K. Shirai, and T. Oguchi, Insight into anisotropic magnetocaloric effect of $CrI_3$, Acta Mater. **231**, 117851 (2022).

[24] G. Zhang, J. Yu, H. Wu, L. Yang, W. Jin, B. Xiao, W. Zhang, and H. Chang, Above-room-temperature intrinsic ferromagnetism in ultrathin van der Waals crystal $Fe_{3+x}GaTe_2$, Appl. Phys. Lett. **125**, 121901 (2024).

[25] M. Lopez, P. Yan, P. Y. Zavalij, A. Javadi, I. da Silva, Z. Wang, S. Ren, J. W. Bennett, and E. E. Rodriguez, Evidence of ferrimagnetism in $Fe_3GaTe_2$ via neutron diffraction studies, J. Mater. Chem. C **13**, 15354 (2025).

[26] S. E. Lee, Y. Li, Y. Lee, W. K. Brown, P. Cai, J. Yun, C. Lee, A. Moon, L. Mei, J. Kim, Y. Xin, J. A. Borchers, T. W. Heitmann, M. Frontzek, W. D. Ratcliff, G. T. McCandless, J. Y. Chan, E. J. G. Santos, J. Kim, C. M. Phatak, *et al.*, Local inversion symmetry breaking and thermodynamic evidence for ferrimagnetism in $Fe_3GaTe_2$, ACS Nano **19**, 28702 (2025).

[27] H. Zhang, Y.-T. Shao, X. Chen, B. Zhang, T. Wang, F. Meng, K. Xu, P. Meisenheimer, X. Chen, X. Huang, P. Behera, S. Husain, T. Zhu, H. Pan, Y. Jia, N. Settineri, N. Giles-Donovan, Z. He, A. Scholl, A. N'Diaye, *et al.*, Spin disorder control of topological spin texture, spin disorder control of topological spin texture, Nat. Commun. **15**, 3828 (2024).

[28] L.-Z. Zhang, X.-D. He, A.-L. Zhang, Q.-L. Xiao, W.-L. Lu, F. Chen, Z. Feng, S. Cao, J. Zhang, and J.-Y. Ge, Tunable Curie temperature in layered ferromagnetic $Cr_{5+x}Te_8$ single crystals, APL Mater. **8**, 031101 (2020).

[29] L.-Z. Zhang, Q.-L. Xiao, F. Chen, S. Cao, J. Zhang, and J.-Y. Ge, Multiple magnetic phase transitions and single crystal $Cr_5Te_6$, J. Magn. Magn. Mater. **546**, 168770 (2022).

[30] Y. Liu, J. Li, J. Tao, Y. Zhu, and C. Petrovic, Anisotropic magnetocaloric effect in $Fe_{3-x}GeTe_2$, Sci. Rep. **9**, 13233 (2019).

[31] C. Zhang, Z. Jiang, J. Jiang, W. He, J. Zhang, F. Hu, S. Zhao, D. Yang, Y. Liu, Y. Peng, H. Yang, and H. Yang, Above-room-temperature chiral skyrmion lattice and Dzyaloshinskii-Moriya interaction in a van der Waals ferromagnet $Fe_{3-x}GaTe_2$, Nat. Commun. **15**, 3113 (2024).

[32] J. Jiang, Y. Wu, L. Kong, Y. Zhang, S. Qiu, H. Zhang, Y. Ke, S. Wang, M. Tian, and J. Tang, Stable Néel-twisted skyrmion bags in a van der Waals magnet $Fe_{3-x}GaTe_2$ at room temperature, Nano Lett. **25**, 3282 (2025).

[33] Z.-J. Yan, Z. Wang, B. Xia, S. Paolini, Y.-T. Chan, N. Dihingia, H. Rong, P. Xiao, K. D. Halanayake, J. Song, V. Gowda, D. R. Hickey, W. Wu, J. Yu, P. J. Hirschfeld, and C.-Z. Chang, Stoichiometric FeTe is a superconductor, Nature (London) **652**, 342 (2026).

[34] E. C. Stoner and E. P. Wohlfarth, A mechanism of magnetic hysteresis in heterogeneous alloys, Philos. Trans. A Math. Phys. Eng. Sci. **240**, 599 (1948).

[35] G. Kresse and J. Hafner, *Ab initio* molecular dynamics for liquid metals, Phys. Rev. B **47**, 558 (1993).

[36] G. Kresse and J. Furthmuller, Efficient iterative schemes for *ab initio* total-energy calculations, Phys. Rev. B **54**, 11169 (1996).

[37] J. P. Perdew, K. Burke, and M. Ernzerhof, Generalized gradient approximation made simple, Phys. Rev. Lett. **77**, 3865 (1996).

[38] P. E. Blochl, Projector augmented-wave method, Phys. Rev. B **50**, 17953 (1994).

[39] A. M. Ruiz, D. L. Esteras, D. Lopez-Alcala, and J. J. Baldovi, On the origin of the above-room-temperature magnetism in the 2D van der Waals ferromagnet $Fe_3GaTe_2$, Nano Lett. **24**, 7886 (2024).

[40] A. Rahman, M. U. Rehman, Z. Chen, W. Ahmad, Z. U. Rahman, Y. Yang, M. Ge, and L. Zhang, Multiple spin couplings and layer-valley interactions in room-temperature ferromagnetic $Fe_3GaTe_2$, Front. Phys. **20**, 33201 (2025).

[41] D. Zhang, H. Wei, J. Duan, J. Chen, J. Chen, D. Yue, W. Gong, P. Liu, Y. Yang, J. Gou, J. Yan, K. Zhai, P. Wang, S. Hu, Z. Jia, W. Jiang, L. Liu, W. Wang, Y. Li, and Y. Jiang, Orbital torque switching of room temperature two-dimensional van der Waals ferromagnet $Fe_3GaTe_2$, Nat. Commun. **16**, 7047 (2025).

[42] See Supplemental Material at http://link.aps.org/supplemental/10.1103/k713-wl4g for the comparison of ZFC and FC magnetization curves and the demagnetization effect on magnetic

property measurements; the doping concentration dependence of coercivity for $Fe_3GaTe_2$ single crystals; the refined crystal data for Ni-doped $Fe_3GaTe_2$; the comparison of structural parameters, site-resolved magnetization, and MAE between our ideal-structure calculation and previous literature reports; the spin-resolved band structure of pure $Fe_3GaTe_2$ with different intrinsic defect concentrations; the spin-resolved band structures of $Fe_3GaTe_2$ with different Ni doping concentrations based on the defect lattice; the projected density of states of $Fe_3GaTe_2$ with different intrinsic Fe defect configurations; the projected density of states comparison between the pristine defective Fe configuration and the low Ni doping configuration; and the projected density of states comparison between the high-defect Fe configuration and the high Ni doping configuration, which includes Refs. [22,24–26].

[43] J. Amaral, M. Reis, V. Amaral, T. Mendonc, J. Araujo, M. Sa, P. Tavares, and J. Vieira, Magnetocaloric effect in Er-and Eu-substituted ferromagnetic La-Sr manganites, J. Magn. Magn. Mater. **290-291**, 686 (2005).

[44] M. H. Phan and S. C. Yu, Review of the magnetocaloric effect in manganite materials, J. Magn. Magn. Mater. **308**, 325 (2007).

[45] R. Liang, J. Liu, L. Zhou, and N. Tang, Large relative cooling power in van der Waals room-temperature ferromagnet $Fe_5GeTe_2$, Appl. Phys. Lett. **124**, 182406 (2024).

[46] A. Goswami, N. Ng, A. M. M. Abeykoon, E. Yakubu, and S. Guchhait, High magnetic anisotropy and magnetocaloric effects in single-crystal $Cr_2Te_3$, ACS Appl. Electron. Mater. **6**, 4043 (2024).

[47] Y. Liu, M. Abeykoon, E. Stavitski, K. Attenkofer, and C. Petrovic, Magnetic anisotropy and entropy change in trigonal $Cr_5Te_8$, Phys. Rev. B **100**, 245114 (2019).

[48] Y. Liu and C. Petrovic, Anisotropic magnetocaloric effect in single crystals of $CrI_3$, Phys. Rev. B **97**, 174418 (2018).

[49] Y. Wang, D. Yang, Z. Cheng, J. Wang, J. Liu, Y. Zhang, Y. Wang, Y. Zhang, M. Li, Y. Wu, T. Nie, S. Yang, and G. Han, Strong room-temperature ferromagnetism and magnetocaloric effect in anisotropic two-dimensional chromium indium telluride, Mater. Futures **4**, 035701 (2025).

[50] Y. Liu and C. Petrovic, Anisotropic magnetic entropy change in $Cr_2X_2Te_6$ (X = Si and Ge), Phys. Rev. Mater. **3**, 014001 (2019).

[51] X. Yang, J. Pan, W. Gai, Y. Tao, H. Jia, L. Cao, and Y. Cao, Three-dimensional critical behavior and anisotropic magnetic entropy change in quasi-two-dimensional $LaCrSb_3$, Phys. Rev. B **105**, 024419 (2022).

[52] Z. Lin, L. Q. Zeng, S. Fan, L. Zhang, Y. Chen, J. Yang, and Z. Huang, Critical behavior and large magnetocaloric properties in a van der Waals ferromagnet $CrBr_3$, Phys. Rev. Appl. **23**, 024027 (2025).

[53] A. Goswami, N. Ng, E. Yakubu, and S. Guchhait, Room temperature magnetocaloric effects in monoclinic $Cr_3Te_4$, J. Appl. Phys. **137**, 043909 (2025).

[54] A. Goswami, G. Ye, K. J. Sarkar, C. Nnokwe, A. Alaspa, Z. Sofer, R. He, and S. Guchhait, Rapid shift of the peak of magnetic entropy change driven by strong intralayer ferromagnetic ordering in single crystal CrSBr, Phys. Rev. B **113**, 054444 (2026).

[55] K. Li, X. Tu, X. Sun, H. Bi, Y. Fang, and F. Huang, Ferromagnetic intercalated compounds $CrHf_xTe_2$, J. Mater. Chem. C **13**, 18631 (2025).

[56] J. Ma, F. Meng, W. Liu, M. Ge, A. Wang, L. Ling, J. Fan, C. Ma, L. Pi, Z. Qu, and L. Zhang, Critical phenomenon and two-dimensional Ising magnetic coupling in the chiral magnetic soliton host $Mn_{1/3}TaS_2$, Phys. Rev. B **112**, 094439 (2025).

[57] W. Liu, Y. Wang, J. Fan, L. Pi, M. Ge, L. Zhang, and Y. Zhang, Field-dependent anisotropic magnetic coupling in layered ferromagnetic $Fe_{3-x}GeTe_2$, Phys. Rev. B **100**, 104403 (2019).

[58] K. Rácova, E. Čižmár, and A. Feher, Magnetocaloric effect in $NiCl_2$(bipy) at low temperatures, Acta Phys. Pol. A **131**, 922 (2017).

[59] S. Bera, S. K. Pradhan, M. S. Khan, R. Pal, B. Pal, S. Kalimuddin, A. Bera, B. Das, A. N. Pal, and M. Mondal, Unravelling the nature of spin reorientation transition in quasi-2D vdW magnetic material $Fe_4GeTe_2$, J. Magn. Magn. Mater. **565**, 170257 (2023).

[60] J. Yan, X. Luo, F. C. Chen, J. J. Gao, Z. Z. Jiang, G. C. Zhao, Y. Sun, H. Y. Lv, S. J. Tian, Q. W. Yin, H. C. Lei, W. J. Lu, P. Tong, W. H. Song, X. B. Zhu, and Y. P. Sun, Anisotropic magnetic entropy change in the hard ferromagnetic semiconductor $VI_3$, Phys. Rev. B **100**, 094402 (2019).

[61] V. Franco, J. S. Blazquez, and A. Conde, Field dependence of the magnetocaloric effect in materials with a second order phase transition: A master curve behavior, Appl. Phys. Lett. **89**, 222512 (2006).

[62] A. Arrott, Criterion for ferromagnetism from observations of magnetic isotherms, Phys. Rev. **108**, 1394 (1957).

[63] S. N. Kaul, Static critical phenomena in ferromagnets with quenched disorder, J. Magn. Magn. Mater. **53**, 5 (1985).

[64] J. C. Le Guillou and J. Zinn-Justin, Critical exponents from field theory, Phys. Rev. B **21**, 3976 (1980).

[65] D. Kim, B. Revaz, B. L. Zink, F. Hellman, J. J. Rhyne, and J. F. Mitchell, Tricritical point and the doping dependence of the order of the ferromagnetic phase transition of $La_{1-x}Ca_xMnO_3$, Phys. Rev. Lett. **89**, 227202 (2002).

[66] Y. You, J. Liu, B. Ding, F. Xu, and Z. Sun, Critical behavior and anisotropic magnetocaloric effect in off-stoichiometric van der Waals ferromagnet $Fe_{3-x}GaTe_2$, J. Magn. Magn. Mater. **623**, 172997 (2025).

[67] C. Hu, F. Tang, L. Jiang, Y. Chen, H. Chen, Z. Xia, Y. Fang, H. Xuan, B. Qian, and Z. Han, Anisotropic magnetic entropy change and magnetic critical behavior in van der Waals $Fe_3GaTe_2$, Phys. B **696**, 416615 (2025).

[68] X. B. Shi, N. Zhang, Y. H. Bai, H. Y. Yuan, J. J. Liu, X. Zhang, and B. Wang, The origin of strong perpendicular magnetic anisotropy in a ferromagnetic $Fe_3GaTe_2$ monolayer, Cryst. Growth Des. **25**, 8165 (2025).

[69] X. Li, M. Zhu, Y. Wang, F. Zheng, J. Dong, Y. Zhou, L. You, and J. Zhang, Tremendous tunneling magnetoresistance effects based on van der Waals room-temperature ferromagnet $Fe_3GaTe_2$ with highly spin-polarized Fermi surfaces, Appl. Phys. Lett. **122**, 082404 (2023).

[70] J. Li, S. Liu, C. Wang, F. Ren, B. Wang, and J.-H. Cho, Microscopic origin of the magnetic easy-axis switching in $Fe_3GaTe_2$ under pressure, Phys. Rev. B **112**, 144428 (2025).